Astrophysics
https://doi.org/10.1007/s10511-026-09892-7

THE ORIGIN OF MULTIWAVELENGTH EMISSION FROM PKS 1441+25

Check for updates

Mher Khachatryan[1]

Received: 13 February 2026 / Revised: 13 February 2026 / Accepted: 14 February 2026

Abstract

A multiwavelength study of the flat-spectrum radio quasar PKS 1441+25 ($z = 0.939$), one of the most distant blazars detected in the very-high-energy (VHE; $E > 100$ GeV) γ-ray band, is presented. Using uniformly processed data from the Markarian Multiwavelength Data Center, Fermi-LAT γ-ray data are combined with Swift XRT/UVOT, NuSTAR, and ground-based optical and infrared measurements (ASAS-SN, ZTF, Pan-STARRS, NEOWISE) to characterize the emission from the source in different states. An adaptively binned light curve shows a prolonged high state in the γ-ray band starting around MJD 57000, including a bright γ-ray flare in late January and a hard emission spectrum in April coincident with detection of VHE photons from the source by MAGIC and VERITAS. Using simultaneous data, SEDs are constructed for three characteristic epochs - the bright HE γ-ray flare in January, the April period with MAGIC and VERITAS VHE detections, and the quiescent states in May and June - and modeled within a one-zone external inverse-Compton framework. The theoretical modeling is implemented using novel convolutional neural-network surrogate models which allow full exploration of parameter space. The modeling shows that the April–June SEDs are reproduced by weak magnetic fields and an emission region of size $R \sim 10^{17}$ cm, implying an emitting zone located beyond the broad-line region. In this regime, photons from the dusty torus provide the dominant external field, and internal $\gamma\gamma$ absorption is negligible, allowing VHE photons to escape from the emitting region. In contrast, the January flare is best described by a more strongly magnetized and compact emission region $R \sim 10^{15}$ cm, implying a location much closer to the central black hole, where disk and BLR radiation dominate. Under these conditions, efficient $\gamma\gamma$ absorption suppresses VHE emission despite the higher GeV flux. The results support a scenario in which the 2015 activity of PKS 1441+25 is driven primarily by the relocation and evolution of the dissipation region along the jet rather than by changes in the underlying emission mechanism.

Keywords Blazars, Flat-spectrum radio quasars, Relativistic jets, External inverse Compton, Multiwavelength observations

Introduction

Blazars are the most extreme class of active galactic nuclei (AGNs), characterized by the presence of a relativistic jet closely aligned with the line of sight to the observer [1]. This geometric configuration results in a strong Doppler boosting of the non-thermal jet emission and produces fast and strong variability across the entire electromagnetic spectrum, often on timescales ranging from months down to hours [e.g., 2–5]. Their broad-band emission, strong polarization, and rapid multiwavelength variability make blazars excellent laboratories for studying particle acceleration, jet energetics, and radiative processes in relativistic outflows.

Blazars are generally divided into two subclasses: flat-spectrum radio quasars (FSRQs) and BL Lacertae (BL Lac) objects [1]. FSRQs exhibit strong, broad optical emission lines and generally have luminous accretion disks surrounded by a dense broad-line region (BLR). In contrast, BL Lacs show weak or absent emission lines. Despite their differences, both subclasses show a characteristic double-peaked spectral energy distribution (SED) [6]. The low-energy component, extending from radio to optical/X-rays, is attributed to synchrotron radiation from relativistic electrons in the jet. The origin of the high-energy (HE; $E > 100$ MeV) and very-high-energy (VHE; $E > 100$ GeV) emission is generally explained through inverse Compton (IC) scattering. In BL Lacs, the dominant process is synchrotron self-Compton (SSC) [7–9] process, where synchrotron photons are up-scattered by the same population of electrons. In FSRQs, external inverse Compton (EIC) processes - where external photon fields originating from the accretion disk [10, 11], BLR [12], or dusty torus [13] serve as seed photons for Compton scattering - is the dominant HE emission mechanism.

Observations of blazars in the VHE γ-ray band are of special importance. In this range, mostly BL Lac objects are detected, whereas only a handful of FSRQs have been observed above 100 GeV. This is because the dense external photon

---

Mher Khachatryan
khachatryanmher@fizmat.am

[1] ICRANet-Armenia IO, Marshall Baghramian Avenue 24a, Yerevan 0019, Armenia

fields in FSRQs results to strong absorption of VHE photons through $\gamma\gamma$ pair production. Therefore, for VHE photons to escape, the emission region must typically be outside the BLR.

PKS 1441+25 is one of the very few FSRQs that have been successfully detected in the VHE γ-ray band. MAGIC and VERITAS reported detections during an intense flaring episode in April 2015 [14, 15], revealing emission extending to several hundred GeV. This discovery triggered a multi-instrument observing campaign that resulted in the collection of extensive multiwavelength data. With a redshift of $z = 0.939$, PKS 1441+25 is among the most distant blazars ever detected at VHE energies. At such distances, γ-rays above $\sim$ 100 GeV experience strong attenuation due to interactions with the extragalactic background light (EBL). Consequently, the detections by MAGIC and VERITAS not only probe the particle-acceleration and radiative processes operating within the jet, but also allows to obtain valuable constraints on the EBL density in the near-UV to near-IR regime [14, 15].

Given its detection in the VHE γ-ray band and the availability of extensive multiwavelength observations, PKS 1441+25 offers a unique opportunity to investigate the physical conditions that allow production of the VHE photons in the relativistic jet and to escape from an FSRQ environment. The primary goal of this paper is to carry out a comprehensive multiwavelength study of the source using γ-ray data from the Fermi Large Area Telescope (*Fermi*-LAT), X-ray data from NuSTAR, and X-ray and optical/UV data from the Neil Gehrels Swift Observatory (hereafter Swift), together with additional optical measurements. Then through theoretical modeling of the SEDs across different periods using self-consistent radiative models to investigate the changes in the jet of PKS 1441+25 that yielded the emission of VHE photons.

The paper is structured as follows. The data analysis is presented and discussed in Section “Data analysis”. The theoretical modeling framework and corresponding results are described in Section “Origin of multiwavelength emission from PKS 1441+25”. The discussion is provided in Section “Discussion”, and the conclusions are summarized in Section “Conclusions”.

Data analysis

PKS 1441+25 was monitored across multiple wavelength bands using a combination of ground-based and space-based instruments. The datasets employed in this study are summarized below.

Fermi-LAT γ-ray data

The γ-ray observations from the *Fermi*-LAT are used to examine the emission of PKS 1441+25 in the γ-ray band. The LAT is a pair-conversion instrument operating over an energy range of 20 MeV to 300 GeV and, in its nominal survey mode, scans the entire sky approximately every three hours. A detailed description of the *Fermi*-LAT instrument can be found in [16].

The γ-ray data used in this study were obtained from the Markarian Multiwavelength Data Center [MMDC; 17], which provides uniformly processed data from the observations of the blazars bright in γ-ray band. A complete description of the analysis methodology is given in [17]; here we summarize the essential steps. The analysis follows the standard point-source procedures implemented in the *fermitools* (version 2.0.8) using the P8R3_SOURCE_V3 instrument response functions. Events with high photon probability (*evclass*=128 and *evtype*=3) were selected within a 12° region of interest centered on the γ-ray position of PKS 1441+25 (RA = 220.99°, Dec = 25.02°), covering the interval from 2008 August 4 to 2023 July 4 (MET 239667417–710178221). To reduce contamination from Earth-limb emission, events with zenith angles greater than 90° were excluded. For the binned likelihood analysis, the model included all sources within a 17° radius of the target, as listed in the 4FGL catalog (incremental DR3; [18]). The spectral parameters of sources located inside the 12° region of interest were left free during the fit, whereas those outside this radius were fixed to their catalog values. The model also incorporated the standard Galactic and isotropic diffuse components, using the most recent templates, `gll_iem_v07` and `iso_P8R3_SOURCE_V3_v1`. The significance of the γ-ray emission was evaluated using the test statistic $TS = 2(\ln L_1 - \ln L_0)$, where L_1 and L_0 denote the maximum likelihoods obtained with and without the source included in the model [19].

The γ-ray variability of PKS 1441+25 was investigated using the adaptive binning technique described by [20]. Unlike methods that divide the light curve into fixed time intervals, this approach defines time bins according to the statistical precision of the flux. Consequently, the bins become shorter during bright states-allowing to resolve the rapid variability -and longer during low-flux periods, ensuring sufficient photon statistics. This method enables the detection of flux changes and the identification of distinct emission states. To construct the adaptively binned light curve for PKS 1441+25, the full dataset was segmented into intervals for which the flux uncertainty above the optimal energy threshold $E_{\rm opt} = 300.2$ MeV reaches 20%. For each resulting bin, a standard unbinned likelihood analysis was performed using the same cuts described above. Within these shorter intervals, the spectrum of PKS 1441+25 was modeled with a simple power law, which provides an adequate representation of the γ-ray emission on such timescales.

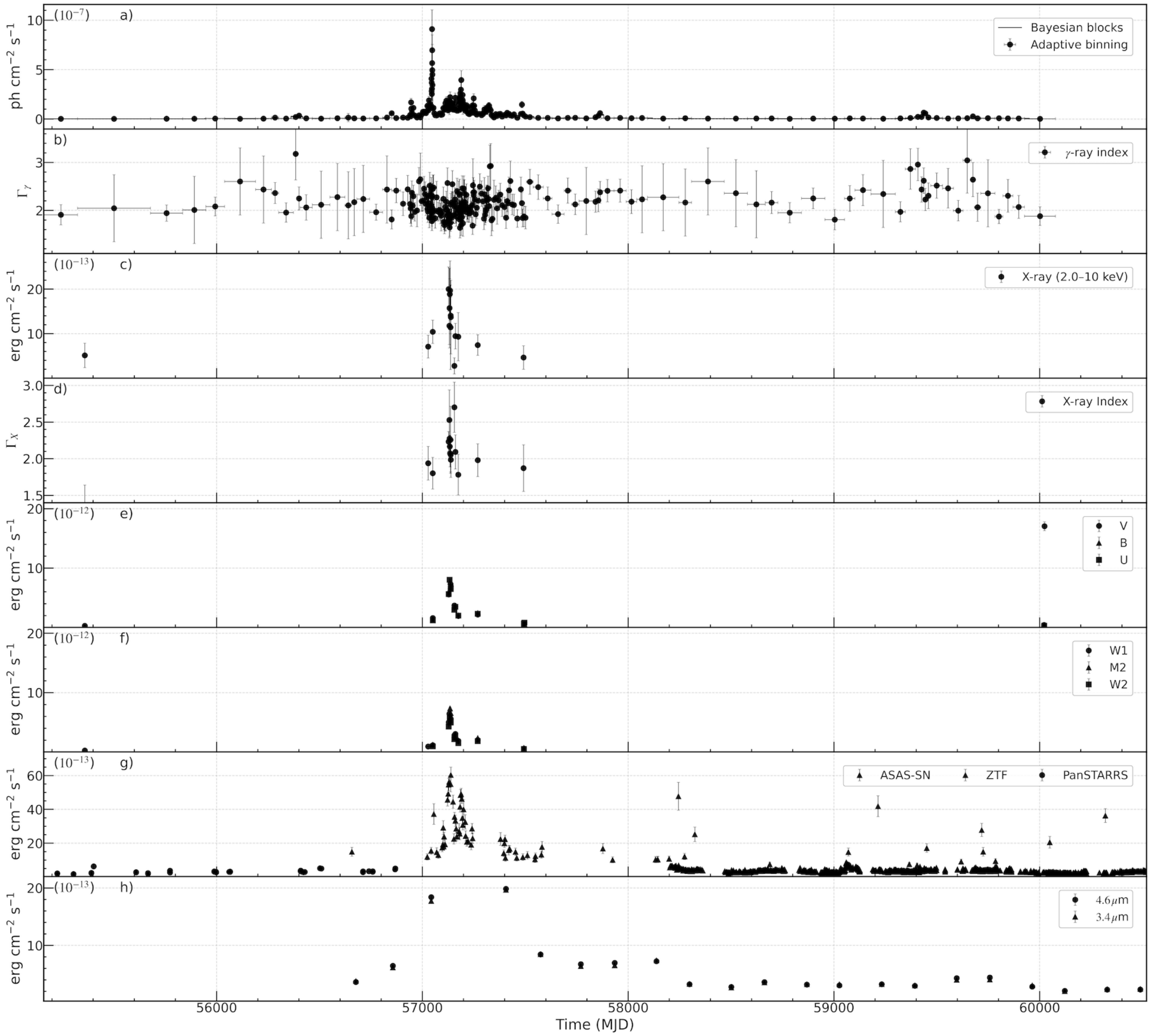

Fig. 1 Multiwavelength light curves of PKS 1441+25 from 2008 to 2023. (a) Adaptively binned *Fermi*-LAT flux above 300.2 MeV, with the Bayesian-block representation of the light curve (solid line), (b) γ-ray photon index, (c) Swift-XRT 2–10 keV flux, (d) X-ray photon index in the 0.3–10 keV band, (e) Swift UVOT optical fluxes in the V (circles), B (triangles), and U (squares) filters, (f) Swift UVOT ultraviolet fluxes in the W1 (circles), M2 (triangles), and W2 (squares) filters, (g) Optical fluxes from ASAS-SN (triangles), ZTF (points), and Pan-STARRS (pentagons), (h) NEOWISE infrared fluxes at 4.6 μm (circles) and 3.4 μm (triangles). The pronounced high state around MJD 57000 is contemporaneous across the γ-ray, X-ray, optical/UV, and infrared bands.

The γ-ray light curve is shown in Figure 1, panel (a). The source exhibits enhanced γ-ray activity beginning around MJD 57000. The highest flux above 100 MeV was measured on MJD 57046.91, reaching $(9.11 \pm 1.93) \times 10^{-7}$ ph cm^{-2} s^{-1}. During this interval, the γ-ray photon index was 2.27 ± 0.24. While additional periods of elevated γ-ray activity are present, this episode represents the strongest γ-ray flare of PKS 1441+25 within the time range considered. The temporal evolution of the photon index is shown in Figure 1, panel (b). The mean γ-ray photon index over the entire dataset is $\Gamma_{\mathrm{mean}} = 2.15$, although the spectrum occasionally hardens significantly. The hardest index, 1.64 ± 0.21, was observed on MJD 57182.82. In total, 41 time bins exhibit a hard spectrum with $\Gamma < 1.9$. Notably, during the period when VHE γ-ray emission from PKS 1441+25 was detected (20–27 April) [14, 15], the HE-band photon index remained hard ($\Gamma < 2.0$) for most of the time.

X-ray band

In the X-ray band, the emission from PKS 1441+25 was examined using Swift-XRT observations in the 0.3–10 keV range and NuSTAR data covering 3–79 keV.

In the Swift archive, 29 observations of PKS 1441+25 are available. These data-along with X-ray observations of all blazars by Swift-have been uniformly processed and are made publicly accessible through MMDC. A full description of the X-ray data analysis procedure is provided in [17]; here we summarize the steps relevant to the present work. The analysis was performed with the *Swift_xrtproc* tool [21], which builds on XRTDAS and uses XSPEC and XIMAGE to implement the standard reduction methods required for analyzing Swift-XRT data. For each observation, the tool automatically retrieves the archival dataset, applies event cleaning and filtering, and generates calibrated Level-2 products. Source counts are extracted from a circular region with a radius of 20 pixels ($\sim$ 47 arcsec), while the background is estimated from a nearby source-free region with a radius of 40 pixels. To check for possible pile-up, the count rate of each observation was inspected, and datasets exceeding 0.5 count s^{-1} were corrected following [21]. The spectra were grouped with GRPPHA to ensure at least one count per bin and then imported into XSPEC [22] for fitting using Cash statistics [23]. Both power-law and log-parabola models were tested, adopting a fixed Galactic hydrogen column density of 3.11×10^{20} cm^{-2}. From the final spectral fits, we obtained the photon index and flux measurements in different X-ray bands for each observation.

The time evolution of the 2–10 keV X-ray flux is shown in Figure 1, panel (c). Most X-ray observations were carried out between MJD 57000 and 58000, coinciding with the period when the source exhibited enhanced γ-ray-band activity. The highest X-ray flux, $(2.00 \pm 0.50) \times 10^{-12}$ erg cm^{-2} s^{-1}, was observed on MJD 57127.5, exceeding by a factor of 7.3 the lowest flux of $(2.73 \pm 1.81) \times 10^{-13}$ erg cm^{-2} s^{-1} observed on MJD 57155.3. The temporal evolution of the photon index in the 0.3–10 keV range is presented in Figure 1, panel (d). The mean photon index is 2.05, with values spanning from a minimum of 1.78 ± 0.28 to a maximum of 2.74 ± 0.34. The observed variability in the photon index-ranging from relatively hard $\Gamma \approx 1.8$ to distinctly soft $\Gamma \approx 2.7$-suggests that the X-ray band in PKS 1441+25 can probe different parts of the broadband emission. Harder spectra are consistent with sampling the rising portion of the inverse Compton component or the transition region between synchrotron and inverse Compton components, while softer indices shows the X-ray band is the highest tail of the synchrotron component.

NuSTAR, operating in the 3–79 keV band with its two focal-plane modules (FPMA and FPMB), observed PKS 1441+25 on 2015 April 25. The data were retrieved from MMDC, where all data from NuSTAR observations of blazars are uniformly processed and made publicly available [17]. A detailed description of the NuSTAR data-analysis is provided in [17]; here we summarize the steps relevant to this work. The analysis was performed using the *NuSTAR_Spectra* pipeline [24], which downloads the raw event files, applies standard NuSTAR calibration and screening, and produces science-ready products through the *nuproducts* task. Source photons were extracted from a circular region centered on the source, while background events were taken from an annular region centered on the same position. The radii of the extraction regions were automatically optimized by the pipeline based on the observed count rate, ensuring adequate signal-to-noise in both bright and faint states. The spectra from FPMA and FPMB were then imported into XSPEC [22] and fitted jointly using both power-law and log-parabola models, with Galactic absorption included. Cash statistics [23] were adopted to determine the best-fitting spectral parameters.

The NuSTAR observation yields a 3–10 keV flux of $(7.88 \pm 0.32) \times 10^{-12}$ erg cm^{-2} s^{-1} and a 10–30 keV flux of $(5.85 \pm 0.41) \times 10^{-12}$ erg cm^{-2} s^{-1}. The spectrum is relatively soft, with a photon index of 2.18 ± 0.12. This observation coincides with a Swift-XRT observation on the same day, for which a photon index of 2.05 ± 0.24 was measured. The combined Swift and NuSTAR data therefore provide continuous coverage of the X-ray spectrum from 0.3 to 30 keV, enabling a consistent characterization of the spectral shape across the soft and hard X-ray bands.

optical/UV band

Together with the Swift XRT observations, PKS 1441+25 was monitored in the optical (V: 500–600 nm, B: 380–500 nm, U: 300–400 nm) and ultraviolet (W1: 260–400 nm, M2: 200–280 nm, W2: 180–260 nm) bands using the Ultra-Violet/Optical Telescope [UVOT; 25] on board Swift [26]. The UVOT data are retrieved from MMDC, where all Swift UVOT blazar observations are uniformly processed and publicly released [17]. A detailed description of the reduction procedure is provided in [17]; here we summarize the key steps relevant to this work. The data were reduced following the standard UVOT data analysis using HEAsoft v6.29 and the latest HEASARC CALDB. Source counts were extracted from a 5-arcsec circular region, while the background was estimated from a nearby 20-arcsec region free of contaminating sources. Count rates were converted into fluxes using the UVOT calibration from [27]. Extinction corrections were applied adopting a reddening value of $E(B-V) = 0.038$, obtained from the Infrared Science Archive[1].

In addition to the Swift UVOT observations, MMDC provides additional optical data. Specifically, V- and g-band photometry from ASAS-SN [28] was obtained by querying the public archive within a 5-arcsecond radius around the position of PKS 1441+25. Likewise, photometric measurements in the g, r, and i bands from ZTF [29], as well as g, r, i, z,

---

[1] http://irsa.ipac.caltech.edu/applications/DUST/

and y data from Pan-STARRS [30], were retrieved using a 5-arcsecond cone search. The details of these queries, along with the extinction-correction procedure applied to the data sets, are described in [17].

The resulting optical and UV light curves are shown in Fig. 1, panels (e)–(g). In the optical/UV bands the same general trend seen in the γ-ray and X-ray light curves is present: the source enters a brightening phase beginning around MJD 57000. During this interval, the Swift UVOT observations show a pronounced increase in flux, with the highest value of $(8.03 \pm 0.18) \times 10^{-12}$ erg cm^{-2} s^{-1} measured in the U filter at MJD 57132.24. Across this active period, a large fraction of the UVOT measured fluxes exceed 10^{-12} erg cm^{-2} s^{-1}. The enhanced optical activity is most evident in panel (g), where the Pan-STARRS and ZTF data indicate that the source remained in a relatively low state prior to MJD 57000 and again after MJD 58000, while the ASAS-SN measurements show a clear brightening between MJD 57000 and 57300. The highest flux in the ASAS-SN data is $(1.05 \pm 0.16) \times 10^{-11}$ erg cm^{-2} s^{-1} observed at MJD 60098.35.

In addition to the optical data shown in Fig. 1, panels (e)–(g), the infrared (IR) emission of PKS 1441+25 was examined using observations from the Near-Earth Object Wide-field Infrared Survey Explorer [NEOWISE; 31]. The NEOWISE measurements, retrieved from MMDC [17], include only the 3.4 and 4.6μm bands. Because NEOWISE obtains data in short intervals repeated every six months, measurements separated by less than 10 days were combined using a weighted mean to improve the temporal sampling. The resulting IR light curve is shown in Fig. 1, panel (h), which reveals that the source entered a bright state between MJD 57000–57500. During this interval, the flux peaked at $(3.23\pm0.02)\times10^{-12}$ erg cm^{-2} s^{-1}, while in its typical state the flux remains in the range $(2.00–3.00) \times 10^{-13}$ erg cm^{-2} s^{-1}. These IR measurements are particularly important because [32] demonstrated that the spectral slope between 3.4 and 4.6μm provides a predictor for the synchrotron peak frequency in blazar SEDs. Thus, variations in the IR flux and spectral slope may reflect changes in the synchrotron component of PKS 1441+25 emission.

Origin of multiwavelength emission from PKS 1441+25

The multiwavelength light curve shown in Fig. 1 illustrates the temporal evolution of PKS 1441+25 and provides a basis for defining distinct intervals for theoretical modeling. To increase the statistical quality of the γ-ray spectra, the light curve is segmented into intervals of approximately constant flux using the Bayesian Blocks algorithm (solid line in Fig. 1 panel a). This procedure groups observations with similar flux levels, and the resulting merged data sets yield spectra that extend to higher energies, which is essential for robust theoretical modeling. For each Bayesian Block interval, we also search for contemporaneous multiwavelength observations, then investigate the SEDs with contemporaneous data. Based on this approach, the following periods were selected for detailed modeling:

- **29–30 January**: a period of enhanced HE γ-ray activity with simultaneous Swift coverage.
- **24 April–28 April**: an interval coincident with Swift and NuSTAR observations, as well as VHE γ-ray detections by VERITAS.
- **01–15 May and 01–04 June**: two intervals during which the source remained in a quiescent state across all monitored bands.

Selecting intervals that span both active and quiescent states enables investigation of the physical changes in the jet that give rise to emission extending into the VHE γ-ray band.

Theoretical Modeling

The SEDs corresponding to the selected periods are modeled within a one-zone external inverse Compton (EIC) framework, commonly adopted for FSRQs [10–13]. In this scenario, the low-energy component is produced by synchrotron radiation from relativistic electrons, while the high-energy component arises from inverse Compton scattering of both synchrotron photons (SSC) and external photon fields. The latter may include radiation from the accretion disk, photons reprocessed in the broad-line region (BLR), and infrared emission from the dusty torus.

The modeling is performed through MMDC using the neural-network–based methodology presented in [33]. This approach replaces computationally expensive numerical calculations with a convolutional neural network (CNN) trained on physically motivated radiative simulations, enabling efficient and self-consistent modeling of blazar broadband emission, including particle injection and cooling. Similar surrogate-modeling strategies for SSC scenarios and lepto-hadronic cases are described in [34] and [35], respectively. Here, a brief description of the CNN-based method is provided, and a a full description is provided in [33] for a full description.

Parameter	29–30 Jan 2015	24–28 Apr 2015	01–15 May 2015	01–04 Jun 2015
p	2.40 ± 0.52	2.41 ± 0.20	2.33 ± 0.29	2.38 ± 0.35
$\log \gamma_{\rm cut}$	3.71 ± 1.21	4.94 ± 0.19	5.04 ± 0.42	4.41 ± 0.96
δ	42.62 ± 8.04	45.36 ± 7.46	32.47 ± 7.85	39.53 ± 6.97
$\log B$	0.77 ± 0.26	-1.66 ± 0.36	-1.74 ± 0.50	-1.79 ± 0.80
$\log R$	15.03 ± 0.91	17.10 ± 0.44	17.17 ± 0.44	17.13 ± 0.52
$\log L_{\rm e}$	44.98 ± 0.83	45.99 ± 0.24	45.92 ± 0.56	46.08 ± 0.58
$\log L_{\rm B}$	44.43	43.77	43.46	43.44

Table 1 Best–fit physical parameters obtained from modeling the spectral energy distributions of PKS 1441+25 during the four different periods. For each interval, the table lists the electron injection index p, the cutoff Lorentz factor $\gamma_{\rm cut}$, the Doppler factor δ, the magnetic-field strength B, the radius of the emitting region R, and the electron kinetic luminosity $L_{\rm e}$. The magnetic luminosity $L_{\rm B}$ is computed from the fitted B, R, and δ.

In this model, the electrons are injected into a spherical emission region of radius R, filled with a uniform magnetic field B. The distribution of emitting electrons follows a power law with an exponential cutoff,

$$\dot{Q}(\gamma) = Q_{e,0}\gamma^{-p} \exp\left(-\frac{\gamma}{\gamma_{\rm max}}\right), \tag{1}$$

for $\gamma > \gamma_{\rm min}$, and zero otherwise. Here $Q_{e,0}$ is the normalization defined such that $L_{\rm e} = \pi R^2 \delta^2 m_e c^3 \int_1^\infty \gamma, \dot{Q}(\gamma), d\gamma$, p is the power-law index, $\gamma_{\rm min}$ and $\gamma_{\rm max}$ are the minimum and maximum Lorentz factors, respectively, but the electrons may cool below $\gamma_{\rm min}$. The emission region moves with bulk Lorentz factor Γ and is viewed at an angle $\sim 1/\Gamma$, yielding a Doppler factor $\delta \simeq \Gamma$. The electron interact with both internal synchrotron photons as well as external photons from (i) the accretion disk, (ii) the BLR, and (iii) the dusty torus. The accretion disk is modeled following the standard [36] thin-disk model. The BLR is treated as a spherical shell at

$$R_{\rm BLR} = 10^{17}\ {\rm cm} \left(\frac{L_d}{10^{45}\ {\rm erg\ s^{-1}}}\right)^{1/2}, \tag{2}$$

reprocessing a fraction $f_{\rm BLR} = 0.1$of the disk luminosity and emitting as a black-body spectrum peaking at $\nu_{\rm BLR} = 2.47 \times 10^{15}$ Hz [37]. The dusty torus is modeled as a spherical shell located at

$$R_{\rm DT} = 2.5 \times 10^{18}\ {\rm cm} \left(\frac{L_d}{10^{45}\ {\rm erg\ s^{-1}}}\right)^{1/2}, \tag{3}$$

reprocessing a fraction $f_{\rm DT} = 0.5$ of the disk luminosity and emitting a black-body spectrum peaking at $\nu_{\rm IR} = 3 \times 10^{13}$ Hz.

In this case the model contains nine parameters p, $\gamma_{\rm min}$, $\gamma_{\rm max}$, B, R, δ, $L_{\rm e}$, L_d and the mass of the central supermassive black-hole $M_{\rm BH}$. For very broad range of these parameters, the SEDs are computed using the SOPRANO code [38]. These simulations form the training data set for the CNN, which learns the mapping between physical parameters and the resulting radiative output. The trained network is then used instead of the numerical code to model the observed SEDs.

Modeling results

The CNN-based EIC, SSC, and lepto-hadronic models described above are publicly available through the MMDC data center. The trained neural networks are interfaced with the Bayesian inference framework of MultiNest [39], enabling efficient nested sampling and determination of the parameter sets that best describe the observed SEDs. For all fits, MultiNest was run with 1500 active points and a tolerance of 0.4, ensuring adequate exploration of the parameter space and convergence of the posterior distributions. Because the low-energy (radio/IR) data are sparse or unavailable for the selected periods, we fixed the minimum Lorentz factor to $\gamma_{\rm min} = 100$ during the fit. The accretion disk luminosity was fixed to $L_{\rm d} = 2 \times 10^{45}$ erg s^{-1}, and the black-hole mass to $M_{\rm BH} = 6.76 \times 10^7 M_\odot$. Absorption by the extragalactic background light (EBL) is included by adopting the model of [40].

The modeled SEDs for the four activity periods are shown in Fig. 2, and the corresponding best-fit parameters are summarized in Table 1. All intervals can be reproduced within a one-zone EIC framework, but the physical conditions inferred from the fits vary in a systematic way across the epochs. During the quiescent period between 1–15 May (Fig. 2 left bottom panel), the SED is explained by a moderately energetic electron population with a relatively high cutoff

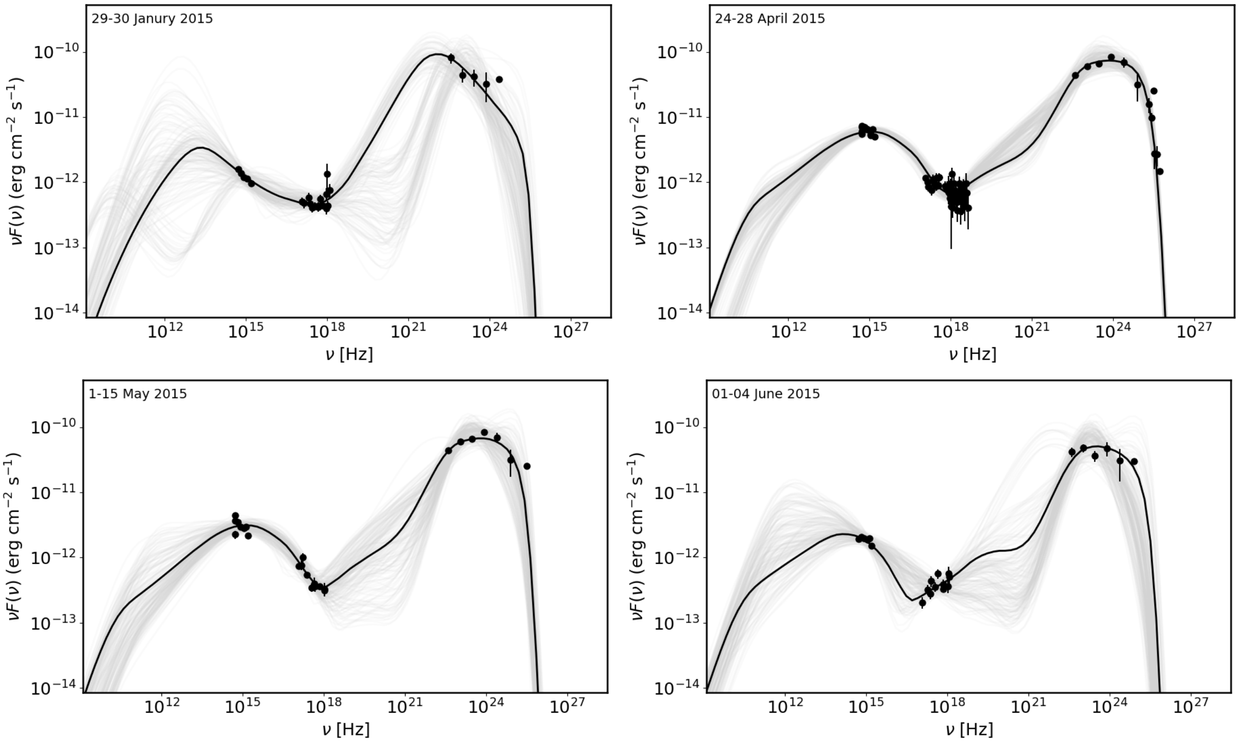

Fig. 2 SED of PKS 1441+25 for the four different intervals selected from the multiwavelength light curve: 29–30 January 2015, 24–28 April 2015, 01–15 May 2015, and 01–04 June 2015. Black points show the contemporaneous multiwavelength data used in each fit. The solid black curve in each panel represents the best–fit one–zone EIC model obtained with the CNN–accelerated inference framework, while the grey curves correspond to random posterior realizations from the MultiNest sampling.

energy, $\log\gamma_{\rm cut}\simeq 5.0$ so that the HE tail of the synchrotron components can reach X-ray band, and a Doppler factor of about 32.5. The magnetic field is weak $\log B\approx -1.7$, and the emitting region is comparatively large $\log R\approx 17.2$. These conditions implies that the source emission is Compton-dominated, where the external radiation field efficiently boosts the inverse-Compton component without requiring either strong magnetic fields or extremely compact emission zones can explain the observed HE γ-ray data.

In the 1–4 June interval (Fig. 2 right bottom panel), the overall SED shape remains similar but with X-ray data describing the increasing part of tye inverse Compton component (SSC). This is case the fit yields an increase in the bulk motion of the emitting region, with the Doppler factor rising to ~ 40. At the same time, the electron energy distribution shifts toward slightly lower cutoff energies ($\log\gamma_{\rm cut}\simeq 4.4$ versus $\log\gamma_{\rm cut}\simeq 5.0$). Despite this reduction, the higher Doppler boosting allows the inverse Compton scattering of the external photon fields to explain the HE γ-ray data. The magnetic field is low and comparable to the value estimated in modeling the SED in May, but the electron luminosity increases, suggesting that the enhanced emission is primarily driven by a larger number of radiating electrons rather than changes in geometry or magnetization.

The changes in the SED are observed during the flaring periods. The SED during 29–30 January (Fig. 2 left upper panel) episode shows a different set of parameters required to explain the SED. Here, the model requires a much more compact emitting region (with $\log R\approx 15$) and a significantly stronger magnetic field of $\log B\approx 0.8$. Such a configuration naturally shifts more power into the synchrotron component and can accommodate rapid variability. The Doppler factor remains high ~ 43, but the cutoff energy is lower and less well constrained due to the more limited X-ray coverage in this interval. This combination of compact size and enhanced magnetization distinguishes this SED modeling from all other periods.

The SED observed during 24–28 April SED when also VHE γ-ray emission were observed from PKS 1441+25 is shown in Fig. 2 right upper panel. The emitting region size and magnetic field are similar to the quiescent state, but the Doppler factor increases to ~ 45, and the electron luminosity is slightly higher. The cutoff energy is well determined and close to $\log\gamma_{\rm cut}\approx 4.9$, producing a HE peak that extends also to VHE γ-ray band. Therefore in this period the enhanced boosting strengthens the HE component without substantial changes in the underlying magnetic or geometric conditions.

The multi-epoch modeling presented here is consistent with earlier modeling of PKS 1441+25, but it shows a more clear picture of how the jet conditions changes in different periods. A direct comparison between the parameters obtained here and those reported in previous modeling efforts is not possible because (i) different data sets were used, and *(ii)* the fits presented here rely on Bayesian nested sampling, whereas earlier studies typically employed local minimization procedures or even qualitative, by-eye adjustments. For example, [15] showed that during April the emission zone must have been located well outside the BLR so the 200 GeV can escape from the region which would be otherwise be absorbed by BLR photons. Their modeling required a relatively large emitting region and weak magnetic field, conditions similar with those inferred from the modeling of SEDs in April, May, and June which yielded extended, low-B, Compton-dominated regions. Similarly, [41] also showed that the April flare was associated with a hardened electron distribution and increased Compton dominance, which was interpreted as either an increase in the bulk Lorentz factor or enhanced magnetic fields within an emission region already located beyond the BLR.

Discussion

The multi-epoch modeling reveals clear differences in the physical conditions of the emission region across the 2015 activity periods of PKS 1441+25. In the current modeling approach the emission-region radius, R, inferred directly from the SED fits is linked with the the distance of the emitting zone from the central black hole. Importantly, we did not impose any prior assumption about the location of the emitting region; rather, the fits naturally converged to different values of R for each epoch, allowing to infer the dominant external radiation fields contributing to the EIC component as well as the possible location of the emission region.

For the three SEDs observed during April, May, and June, the modeling results in a large emission-region radii, with $\log R \sim 17$. Such sizes correspond to distances well beyond the radius of the BLR. For a disk luminosity of $L_{\rm d} = 2 \times 10^{45}$ erg s^{-1}, the BLR is expected to extend to $R_{\rm BLR} \simeq 10^{17}$ cm, after which the energy density of BLR photons drops rapidly. At these larger distances, the dominant external photon field becomes the infrared radiation from the dusty torus. The SEDs of April–June display spectral shapes that are fully consistent with this picture: the inverse-Compton peak is bright and smooth, without signatures of γ-ray attenuation, and the magnetic fields remain weak, placing the source in a Compton-dominated regime typical of emission occurring outside the BLR. These epochs therefore support a scenario in which the dissipation region is located beyond the BLR and interacts primarily with torus photons.

The SED during the flare in January differs from this pattern. In this epoch, the modeling shows a smaller emitting-region radius, implying a location significantly closer to the central engine. At such distances—well inside 10^{17} cm-the energy density of external fields is dominated by direct accretion-disk radiation (mostly) and its reprocessed component from the BLR. In this case, the disk photon fields plays an important role in shaping the HE component, and the reduced distance naturally explains the spectral differences compared to the SEDs from the other periods. In this case, although the γ-ray flux increases, the spectrum remains soft and does not extend into the VHE regime—a behavior naturally expected if VHE photons are absorbed within the BLR, supporting a scenario in which the emission region is located inside the BLR. The January emission zone therefore appears to represent an earlier, upstream dissipation event occurring at a location where the disk and BLR contributions are non-negligible.

Together, these results suggest an evolution of the emitting region along the jet: a compact, magnetically stronger zone located closer to the black hole during the January event, followed by dissipation episodes occurring farther in April–June where the torus radiation field dominates. This interpretation is physically consistent with both the change in SED shapes and the systematic increase in R inferred from the modeling. The smooth transition across these epochs indicates that PKS 1441+25 did not undergo a change in the emission mechanism but rather a shift in the location of the dissipation region, naturally producing the observed differences in Compton dominance, spectral hardness, and variability properties.

This scenario is further supported by the jet energetics. The electron kinetic power, $L_{\rm e}$, shows a systematic increase for the SED obtained in January 2015 compared with the SEDs modeled for April–June. During the latter periods, $L_{\rm e}$ reaches values of order 10^{46} erg, s^{-1}, while the magnetic power, computed as $L_{\rm B} = \pi c R_b^2 \Gamma^2 U_B$, remains almost an order of magnitude lower in these three states, showing a strongly particle-dominated jet once the emission zone moves beyond the BLR, consistent with the weak magnetic fields inferred for these epochs and suggesting that most of the radiative output is carried by a high density of relativistic electrons rather than by magnetic energy. The January episode differs in this respect: the compact emission region and substantially stronger magnetic field yield a magnetic power comparable to the electron power, making the jet closer to equipartition during this early phase. Such elevated magnetization is naturally expected if dissipation occurs close to the black hole, where the jet is still undergoing collimation and accelerating. The transition from the moderately magnetized January state to the particle-dominated April–June states therefore shows not just a change in emitting-region location but also a redistribution of energy within the jet as it expands and interacts with different external radiation fields.

Straive Journal: 10511 Article No.: 9892 TYPESET DISK LE CP Disp.: 2026/3/18 Pages: 13 Layout: Special

Conclusions

In this work a multiwavelength study of PKS 1441+25 is presented combining *Fermi*-LAT γ-ray data, Swift XRT/UVOT and NuSTAR observations, and ground-based optical and infrared photometry, all uniformly processed and accessed through MMDC. The adaptive-binning analysis of the *Fermi*-LAT loight curve shows that the source entered a prolonged high state starting around MJD 57000, during which it exhibited a major HE γ-ray flare in late January and a hard spectra in April when VHE emission from the source were observed. The X-ray, optical/UV, and IR bands show correlated brightening over the same interval, indicating that the entire jet emission zone underwent significant changes in this period.

Dividing the γ-ray light curve into intervals using Bayesian Block algorithm, SEDs from four intervals were selected and modeled within a one-zone EIC framework using novel CNN based method. This approach allowed to efficiently explore the parameter space and to derive posterior distributions for the physical parameters governing the emitting region. For the three SEDs obtained in April, May, and June, the modeling yields large emission-region radii, $\log R \sim 17$, weak magnetic fields, and electron kinetic powers exceeding the magnetic power by almost an order of magnitude. These conditions correspond to dissipation occurring well outside the BLR, where the energy density of BLR photons has already declined and the infrared radiation from the dusty torus dominates the external photon field. The resulting SEDs are strongly Compton-dominated, with smooth high-energy components extending into the VHE band during the April interval, consistent with the detection of VHE γ rays from PKS 1441+25 and with previous single-epoch modeling of the April flare.

The January flare displays a different set of physical conditions. In this epoch the fits resulted in a smaller emission region, $\log R \sim 15$, and a substantially stronger magnetic field, such that the magnetic and electron powers are closer to equipartition. At these smaller radii the dominant external fields are the direct accretion-disk radiation and its reprocessed component in the BLR. The soft HE spectrum and the absence of VHE emission are naturally explained if the emitting region is located inside the BLR, where γ–γ absorption suppresses the escape of the highest-energy photons. This is the most likely reason why, despite the January episode being significantly brighter in the γ-ray band than the later activity periods, no VHE photons were detected.

These results support a picture in which the 2015 activity of PKS 1441+25 is a results not only a change of the emission mechanism, but by a relocation and evolution of the dissipation region along the jet. The jet appears to transition from a compact, near-equipartition zone at distances with the BLR close to the central source, to an extended, particle-dominated region beyond the BLR, with the dominant external photon field changing from disk/BLR to torus radiation. This evolution naturally accounts for the observed differences in Compton dominance, spectral hardness, and variability, and provides a self-consistent explanation for the occurrence of VHE emission only during the April episode.

Section title of first appendix

An appendix contains supplementary information that is not an essential part of the text itself but which may be helpful in providing a more comprehensive understanding of the research problem or it is information that is too cumbersome to be included in the body of the paper.

Acknowledgements. I would like to thank N. Sahakyan for helpful discussions and constructive suggestions. This work was supported by the Science Committee of RA, in the frames of the research project No 24AA-1C039.

Author Contributions. M. Khachatryan wrote the main manuscript.

Data Availability. No datasets were generated or analysed during the current study.

Declarations

Competing interests. The author declares no competing interests.

References

1. Urry, C.M., Padovani, P.: Unified Schemes for Radio-Loud Active Galactic Nuclei. PASP **107**, 803 (1995) https://doi.org/10.1086/133630 arXiv:astro-ph/9506063 [astro-ph]

2. Ackermann, M., Anantua, R., Asano, K., Baldini, L., Barbiellini, G., Bastieri, D., Becerra Gonzalez, J., Bellazzini, R., Bissaldi, E., Blandford, R.D., Bloom, E.D., Bonino, R., Bottacini, E., Bruel, P., Buehler, R., Caliandro, G.A., Cameron, R.A., Caragiulo, M., Caraveo, P.A., Cavazzuti, E.,

Cecchi, C., Cheung, C.C., Chiang, J., Chiaro, G., Ciprini, S., Cohen-Tanugi, J., Costanza, F., Cutini, S., D'Ammando, F., de Palma, F., Desiante, R., Digel, S.W., Di Lalla, N., Di Mauro, M., Di Venere, L., Drell, P.S., Favuzzi, C., Fegan, S.J., Ferrara, E.C., Fukazawa, Y., Funk, S., Fusco, P., Gargano, F., Gasparrini, D., Giglietto, N., Giordano, F., Giroletti, M., Grenier, I.A., Guillemot, L., Guiriec, S., Hayashida, M., Hays, E., Horan, D., Jóhannesson, G., Kensei, S., Kocevski, D., Kuss, M., La Mura, G., Larsson, S., Latronico, L., Li, J., Longo, F., Loparco, F., Lott, B., Lovellette, M.N., Lubrano, P., Madejski, G.M., Magill, J.D., Maldera, S., Manfreda, A., Mayer, M., Mazziotta, M.N., Michelson, P.F., Mirabal, N., Mizuno, T., Monzani, M.E., Morselli, A., Moskalenko, I.V., Nalewajko, K., Negro, M., Nuss, E., Ohsugi, T., Orlando, E., Paneque, D., Perkins, J.S., Pesce-Rollins, M., Piron, F., Pivato, G., Porter, T.A., Principe, G., Rando, R., Razzano, M., Razzaque, S., Reimer, A., Scargle, J.D., Sgrò, C., Sikora, M., Simone, D., Siskind, E.J., Spada, F., Spinelli, P., Stawarz, L., Thayer, J.B., Thompson, D.J., Torres, D.F., Troja, E., Uchiyama, Y., Yuan, Y., Zimmer, S.: Minute-timescale >100 MeV γ-Ray Variability during the Giant Outburst of Quasar 3C 279 Observed by Fermi-LAT in 2015 June. ApJ **824**(2), 20 (2016) https://doi.org/10.3847/2041-8205/824/2/L20 arXiv:1605.05324 [astro-ph.HE]

3. Shukla, A., Mannheim, K., Patel, S.R., Roy, J., Chitnis, V.R., Dorner, D., Rao, A.R., Anupama, G.C., Wendel, C.: Short-timescale γ-Ray Variability in CTA 102. ApJ **854**(2), 26 (2018) https://doi.org/10.3847/2041-8213/aaacca

4. Aleksić, J., Ansoldi, S., Antonelli, L.A., Antoranz, P., Babic, A., Bangale, P., Barrio, J.A., González, J.B., Bednarek, W., Bernardini, E., Biasuzzi, B., Biland, A., Blanch, O., Bonnefoy, S., Bonnoli, G., Borracci, F., Bretz, T., Carmona, E., Carosi, A., Colin, P., Colombo, E., Contreras, J.L., Cortina, J., Covino, S., Da Vela, P., Dazzi, F., De Angelis, A., De Caneva, G., De Lotto, B., Wilhelmi, E.d.O., Mendez, C.D., Prester, D.D., Dorner, D., Doro, M., Einecke, S., Eisenacher, D., Elsaesser, D., Fonseca, M.V., Font, L., Frantzen, K., Fruck, C., Galindo, D., López, R.J.G., Garczarczyk, M., Terrats, D.G., Gaug, M., Godinović, N., Muñoz, A.G., Gozzini, S.R., Hadasch, D., Hanabata, Y., Hayashida, M., Herrera, J., Hildebrand, D., Hose, J., Hrupec, D., Idec, W., Kadenius, V., Kellermann, H., Kodani, K., Konno, Y., Krause, J., Kubo, H., Kushida, J., La Barbera, A., Lelas, D., Lewandowska, N., Lindfors, E., Lombardi, S., Longo, F., López, M., López-Coto, R., López-Oramas, A., Lorenz, E., Lozano, I., Makariev, M., Mallot, K., Maneva, G., Mankuzhiyil, N., Mannheim, K., Maraschi, L., Marcote, B., Mariotti, M., Martínez, M., Mazin, D., Menzel, U., Miranda, J.M., Mirzoyan, R., Moralejo, A., Munar-Adrover, P., Nakajima, D., Niedzwiecki, A., Nilsson, K., Nishijima, K., Noda, K., Orito, R., Overkemping, A., Paiano, S., Palatiello, M., Paneque, D., Paoletti, R., Paredes, J.M., Paredes-Fortuny, X., Persic, M., Poutanen, J., Moroni, P.G.P., Prandini, E., Puljak, I., Reinthal, R., Rhode, W., Ribó, M., Rico, J., Garcia, J.R., Rügamer, S., Saito, T., Saito, K., Satalecka, K., Scalzotto, V., Scapin, V., Schultz, C., Schweizer, T., Shore, S.N., Sillanpää, A., Sitarek, J., Snidaric, I., Sobczynska, D., Spanier, F., Stamatescu, V., Stamerra, A., Steinbring, T., Storz, J., Strzys, M., Takalo, L., Takami, H., Tavecchio, F., Temnikov, P., Terzić, T., Tescaro, D., Teshima, M., Thaele, J., Tibolla, O., Torres, D.F., Toyama, T., Treves, A., Uellenbeck, M., Vogler, P., Zanin, R., Kadler, M., Schulz, R., Ros, E., Bach, U., Krauß, F., Wilms, J.: Black hole lightning due to particle acceleration at subhorizon scales. Science **346**(6213), 1080–1084 (2014) https://doi.org/10.1126/science.1256183 arXiv:1412.4936 [astro-ph.HE]

5. Aharonian, F., Akhperjanian, A.G., Bazer-Bachi, A.R., Behera, B., Beilicke, M., Benbow, W., Berge, D., Bernlöhr, K., Boisson, C., Bolz, O., Borrel, V., Boutelier, T., Braun, I., Brion, E., Brown, A.M., Bühler, R., Büsching, I., Bulik, T., Carrigan, S., Chadwick, P.M., Clapson, A.C., Chounet, L.-M., Coignet, G., Cornils, R., Costamante, L., Degrange, B., Dickinson, H.J., Djannati-Ataï, A., Domainko, W., Drury, L.O., Dubus, G., Dyks, J., Egberts, K., Emmanoulopoulos, D., Espigat, P., Farnier, C., Feinstein, F., Fiasson, A., Förster, A., Fontaine, G., Funk, S., Funk, S., Füßling, M., Gallant, Y.A., Giebels, B., Glicenstein, J.F., Glück, B., Goret, P., Hadjichristidis, C., Hauser, D., Hauser, M., Heinzelmann, G., Henri, G., Hermann, G., Hinton, J.A., Hoffmann, A., Hofmann, W., Holleran, M., Hoppe, S., Horns, D., Jacholkowska, A., de Jager, O.C., Kendziorra, E., Kerschhaggl, M., Khélifi, B., Komin, N., Kosack, K., Lamanna, G., Latham, I.J., Le Gallou, R., Lemière, A., Lemoine-Goumard, M., Lenain, J.-P., Lohse, T., Martin, J.M., Martineau-Huynh, O., Marcowith, A., Masterson, C., Maurin, G., McComb, T.J.L., Moderski, R., Moulin, E., de Naurois, M., Nedbal, D., Nolan, S.J., Olive, J.-P., Orford, K.J., Osborne, J.L., Ostrowski, M., Panter, M., Pedaletti, G., Pelletier, G., Petrucci, P.-O., Pita, S., Pühlhofer, G., Punch, M., Ranchon, S., Raubenheimer, B.C., Raue, M., Rayner, S.M., Renaud, M., Ripken, J., Rob, L., Rolland, L., Rosier-Lees, S., Rowell, G., Rudak, B., Ruppel, J., Sahakian, V., Santangelo, A., Saugé, L., Schlenker, S., Schlickeiser, R., Schröder, R., Schwanke, U., Schwarzburg, S., Schwemmer, S., Shalchi, A., Sol, H., Spangler, D., Stawarz, Ł., Steenkamp, R., Stegmann, C., Superina, G., Tam, P.H., Tavernet, J.-P., Terrier, R., van Eldik, C., Vasileiadis, G., Venter, C., Vialle, J.P., Vincent, P., Vivier, M., Völk, H.J., Volpe, F., Wagner, S.J., Ward, M., Zdziarski, A.A.: An Exceptional Very High Energy Gamma-Ray Flare of PKS 2155-304. ApJ **664**(2), 71–74 (2007) https://doi.org/10.1086/520635 arXiv:0706.0797 [astro-ph]

6. Padovani, P., Alexander, D.M., Assef, R.J., De Marco, B., Giommi, P., Hickox, R.C., Richards, G.T., Smolčić, V., Hatziminaoglou, E., Mainieri, V., Salvato, M.: Active galactic nuclei: what's in a name? A&A Rev. **25**(1), 2 (2017) https://doi.org/10.1007/s00159-017-0102-9 arXiv:1707.07134 [astro-ph.GA]

7. Ghisellini, G., Maraschi, L., Treves, A.: Inhomogeneous synchrotron-self-compton models and the problem of relativistic beaming of BL Lac objects. A&A **146**, 204–212 (1985)

8. Maraschi, L., Ghisellini, G., Celotti, A.: A Jet Model for the Gamma-Ray–emitting Blazar 3C 279. ApJ **397**, 5 (1992) https://doi.org/10.1086/186531

9. Bloom, S.D., Marscher, A.P.: An Analysis of the Synchrotron Self-Compton Model for the Multi–Wave Band Spectra of Blazars. ApJ **461**, 657 (1996) https://doi.org/10.1086/177092

10. Dermer, C.D., Schlickeiser, R., Mastichiadis, A.: High-energy gamma radiation from extragalactic radio sources. A&A **256**, 27–30 (1992)

11. Dermer, C.D., Schlickeiser, R.: On the Location of the Acceleration and Emission Sites in Gamma-Ray Blazars. ApJS **90**, 945 (1994) https://doi.org/10.1086/191929

12. Sikora, M., Begelman, M.C., Rees, M.J.: Comptonization of Diffuse Ambient Radiation by a Relativistic Jet: The Source of Gamma Rays from Blazars? ApJ **421**, 153 (1994) https://doi.org/10.1086/173633

13. Błażejowski, M., Sikora, M., Moderski, R., Madejski, G.M.: Comptonization of Infrared Radiation from Hot Dust by Relativistic Jets in Quasars. ApJ **545**(1), 107–116 (2000) https://doi.org/10.1086/317791 arXiv:astro-ph/0008154 [astro-ph]

14. Ahnen, M.L., Ansoldi, S., Antonelli, L.A., Antoranz, P., Babic, A., Banerjee, B., Bangale, P., Barres de Almeida, U., Barrio, J.A., Bednarek, W.,

Bernardini, E., Biasuzzi, B., Biland, A., Blanch, O., Bonnefoy, S., Bonnoli, G., Borracci, F., Bretz, T., Carmona, E., Carosi, A., Chatterjee, A., Clavero, R., Colin, P., Colombo, E., Contreras, J.L., Cortina, J., Covino, S., Da Vela, P., Dazzi, F., De Angelis, A., De Lotto, B., de Oña Wilhelmi, E., Delgado Mendez, C., Di Pierro, F., Dominis Prester, D., Dorner, D., Doro, M., Einecke, S., Eisenacher Glawion, D., Elsaesser, D., Fernández-Barral, A., Fidalgo, D., Fonseca, M.V., Font, L., Frantzen, K., Fruck, C., Galindo, D., García López, R.J., Garczarczyk, M., Garrido Terrats, D., Gaug, M., Giammaria, P., Godinović, N., González Muñoz, A., Guberman, D., Hahn, A., Hanabata, Y., Hayashida, M., Herrera, J., Hose, J., Hrupec, D., Hughes, G., Idec, W., Kodani, K., Konno, Y., Kubo, H., Kushida, J., La Barbera, A., Lelas, D., Lindfors, E., Lombardi, S., López, M., López-Coto, R., López-Oramas, A., Lorenz, E., Majumdar, P., Makariev, M., Mallot, K., Maneva, G., Manganaro, M., Mannheim, K., Maraschi, L., Marcote, B., Mariotti, M., Martínez, M., Mazin, D., Menzel, U., Miranda, J.M., Mirzoyan, R., Moralejo, A., Moretti, E., Nakajima, D., Neustroev, V., Niedzwiecki, A., Nievas Rosillo, M., Nilsson, K., Nishijima, K., Noda, K., Orito, R., Overkemping, A., Paiano, S., Palacio, J., Palatiello, M., Paneque, D., Paoletti, R., Paredes, J.M., Paredes-Fortuny, X., Persic, M., Poutanen, J., Prada Moroni, P.G., Prandini, E., Puljak, I., Rhode, W., Ribó, M., Rico, J., Rodriguez Garcia, J., Saito, T., Satalecka, K., Schultz, C., Schweizer, T., Shore, S.N., Sillanpää, A., Sitarek, J., Snidaric, I., Sobczynska, D., Stamerra, A., Steinbring, T., Strzys, M., Takalo, L., Takami, H., Tavecchio, F., Temnikov, P., Terzić, T., Tescaro, D., Teshima, M., Thaele, J., Torres, D.F., Toyama, T., Treves, A., Verguilov, V., Vovk, I., Ward, J.E., Will, M., Wu, M.H., Zanin, R., MAGIC Collaboration, Ajello, M., Baldini, L., Barbiellini, G., Bastieri, D., Becerra González, J., Bellazzini, R., Bissaldi, E., Blandford, R.D., Bonino, R., Bregeon, J., Bruel, P., Buson, S., Caliandro, G.A., Cameron, R.A., Caragiulo, M., Caraveo, P.A., Cavazzuti, E., Chiang, J., Chiaro, G., Ciprini, S., D'Ammando, F., de Palma, F., Desiante, R., Di Venere, L., Domínguez, A., Fusco, P., Gargano, F., Gasparrini, D., Giglietto, N., Giordano, F., Giroletti, M., Grenier, I.A., Guiriec, S., Hays, E., Hewitt, J.W., Jogler, T., Kuss, M., Larsson, S., Li, J., Li, L., Longo, F., Loparco, F., Lovellette, M.N., Lubrano, P., Maldera, S., Mayer, M., Mazziotta, M.N., McEnery, J.E., Mirabal, N., Mizuno, T., Monzani, M.E., Morselli, A., Moskalenko, I.V., Nuss, E.: Very High Energy γ-Rays from the Universe's Middle Age: Detection of the z = 0.940 Blazar PKS 1441+25 with MAGIC. ApJ **815**(2), 23 (2015) https://doi.org/10.1088/2041-8205/815/2/L23 arXiv:1512.04435 [astro-ph.GA]

15. Abeysekara, A.U., Archambault, S., Archer, A., Aune, T., Barnacka, A., Benbow, W., Bird, R., Biteau, J., Buckley, J.H., Bugaev, V., Cardenzana, J.V., Cerruti, M., Chen, X., Christiansen, J.L., Ciupik, L., Connolly, M.P., Coppi, P., Cui, W., Dickinson, H.J., Dumm, J., Eisch, J.D., Errando, M., Falcone, A., Feng, Q., Finley, J.P., Fleischhack, H., Flinders, A., Fortin, P., Fortson, L., Furniss, A., Gillanders, G.H., Griffin, S., Grube, J., Gyuk, G., Hütten, M., Håkansson, N., Hanna, D., Holder, J., Humensky, T.B., Johnson, C.A., Kaaret, P., Kar, P., Kelley-Hoskins, N., Khassen, Y., Kieda, D., Krause, M., Krennrich, F., Kumar, S., Lang, M.J., Maier, G., McArthur, S., McCann, A., Meagher, K., Moriarty, P., Mukherjee, R., Nieto, D., O'Faoláin de Bhróithe, A., Ong, R.A., Otte, A.N., Park, N., Perkins, J.S., Petrashyk, A., Pohl, M., Popkow, A., Pueschel, E., Quinn, J., Ragan, K., Ratliff, G., Reynolds, P.T., Richards, G.T., Roache, E., Rousselle, J., Santander, M., Sembroski, G.H., Shahinyan, K., Smith, A.W., Staszak, D., Telezhinsky, I., Todd, N.W., Tucci, J.V., Tyler, J., Vassiliev, V.V., Vincent, S., Wakely, S.P., Weiner, O.M., Weinstein, A., Wilhelm, A., Williams, D.A., Zitzer, B., VERITAS, Smith, P.S., SPOL, Holoien, T.W.-S., Prieto, J.L., Kochanek, C.S., Stanek, K.Z., Shappee, B., ASAS-SN, Hovatta, T., Max-Moerbeck, W., Pearson, T.J., Reeves, R.A., Richards, J.L., Readhead, A.C.S., OVRO, Madejski, G.M., NuSTAR, Djorgovski, S.G., Drake, A.J., Graham, M.J., Mahabal, A., CRTS: Gamma-Rays from the Quasar PKS 1441+25: Story of an Escape. ApJ **815**(2), 22 (2015) https://doi.org/10.1088/2041-8205/815/2/L22 arXiv:1512.04434 [astro-ph.HE]

16. Atwood, W.B., Abdo, A.A., Ackermann, M., Althouse, W., Anderson, B., Axelsson, M., Baldini, L., Ballet, J., Band, D.L., Barbiellini, G., Bartelt, J., Bastieri, D., Baughman, B.M., Bechtol, K., Bédérède, D., Bellardi, F., Bellazzini, R., Berenji, B., Bignami, G.F., Bisello, D., Bissaldi, E., Blandford, R.D., Bloom, E.D., Bogart, J.R., Bonamente, E., Bonnell, J., Borgland, A.W., Bouvier, A., Bregeon, J., Brez, A., Brigida, M., Bruel, P., Burnett, T.H., Busetto, G., Caliandro, G.A., Cameron, R.A., Caraveo, P.A., Carius, S., Carlson, P., Casandjian, J.M., Cavazzuti, E., Ceccanti, M., Cecchi, C., Charles, E., Chekhtman, A., Cheung, C.C., Chiang, J., Chipaux, R., Cillis, A.N., Ciprini, S., Claus, R., Cohen-Tanugi, J., Condamoor, S., Conrad, J., Corbet, R., Corucci, L., Costamante, L., Cutini, S., Davis, D.S., Decotigny, D., DeKlotz, M., Dermer, C.D., de Angelis, A., Digel, S.W., do Couto e Silva, E., Drell, P.S., Dubois, R., Dumora, D., Edmonds, Y., Fabiani, D., Farnier, C., Favuzzi, C., Flath, D.L., Fleury, P., Focke, W.B., Funk, S., Fusco, P., Gargano, F., Gasparrini, D., Gehrels, N., Gentit, F.-X., Germani, S., Giebels, B., Giglietto, N., Giommi, P., Giordano, F., Glanzman, T., Godfrey, G., Grenier, I.A., Grondin, M.-H., Grove, J.E., Guillemot, L., Guiriec, S., Haller, G., Harding, A.K., Hart, P.A., Hays, E., Healey, S.E., Hirayama, M., Hjalmarsdotter, L., Horn, R., Hughes, R.E., Jóhannesson, G., Johansson, G., Johnson, A.S., Johnson, R.P., Johnson, T.J., Johnson, W.N., Kamae, T., Katagiri, H., Kataoka, J., Kavelaars, A., Kawai, N., Kelly, H., Kerr, M., Klamra, W., Knödlseder, J., Kocian, M.L., Komin, N., Kuehn, F., Kuss, M., Landriu, D., Latronico, L., Lee, B., Lee, S.-H., Lemoine-Goumard, M., Lionetto, A.M., Longo, F., Loparco, F., Lott, B., Lovellette, M.N., Lubrano, P., Madejski, G.M., Makeev, A., Marangelli, B., Massai, M.M., Mazziotta, M.N., McEnery, J.E., Menon, N., Meurer, C., Michelson, P.F., Minuti, M., Mirizzi, N., Mitthumsiri, W., Mizuno, T., Moiseev, A.A., Monte, C., Monzani, M.E., Moretti, E., Morselli, A., Moskalenko, I.V., Murgia, S., Nakamori, T., Nishino, S., Nolan, P.L., Norris, J.P., Nuss, E., Ohno, M., Ohsugi, T., Omodei, N., Orlando, E., Ormes, J.F., Paccagnella, A., Paneque, D., Panetta, J.H., Parent, D., Pearce, M., Pepe, M., Perazzo, A., Pesce-Rollins, M., Picozza, P., Pieri, L., Pinchera, M., Piron, F., Porter, T.A., Poupard, L., Rainò, S., Rando, R., Rapposelli, E., Razzano, M., Reimer, A., Reimer, O., Reposeur, T., Reyes, L.C., Ritz, S., Rochester, L.S., Rodriguez, A.Y., Romani, R.W., Roth, M., Russell, J.J., Ryde, F., Sabatini, S., Sadrozinski, H.F.-W., Sanchez, D., Sander, A., Sapozhnikov, L., Parkinson, P.M.S., Scargle, J.D., Schalk, T.L., Scolieri, G., Sgrò, C., Share, G.H., Shaw, M., Shimokawabe, T., Shrader, C., Sierpowska-Bartosik, A., Siskind, E.J., Smith, D.A., Smith, P.D., Spandre, G., Spinelli, P., Starck, J.-L., Stephens, T.E., Strickman, M.S., Strong, A.W., Suson, D.J., Tajima, H., Takahashi, H., Takahashi, T., Tanaka, T., Tenze, A., Tether, S., Thayer, J.B., Thayer, J.G., Thompson, D.J., Tibaldo, L., Tibolla, O., Torres, D.F., Tosti, G., Tramacere, A., Turri, M., Usher, T.L., Vilchez, N., Vitale, V., Wang, P., Watters, K., Winer, B.L., Wood, K.S., Ylinen, T., Ziegler, M.: The Large Area Telescope on the Fermi Gamma-Ray Space Telescope Mission. ApJ **697**(2), 1071–1102 (2009) https://doi.org/10.1088/0004-637X/697/2/1071 arXiv:0902.1089 [astro-ph.IM]

17. Sahakyan, N., Vardanyan, V., Giommi, P., Bégué, D., Israyelyan, D., Harutyunyan, G., Manvelyan, M., Khachatryan, M., Dereli-Bégué, H., Gasparyan, S.: Markarian Multiwavelength Data Center (MMDC): A Tool for Retrieving and Modeling Multitemporal, Multiwavelength, and Multimessenger Data from Blazar Observations. AJ **168**(6), 289 (2024) https://doi.org/10.3847/1538-3881/ad8231 arXiv:2410.01207 [astro-ph.HE]

18. Abdollahi, S., Acero, F., Baldini, L., Ballet, J., Bastieri, D., Bellazzini, R., Berenji, B., Berretta, A., Bissaldi, E., Blandford, R.D., Bloom, E., Bonino, R., Brill, A., Britto, R.J., Bruel, P., Burnett, T.H., Buson, S., Cameron, R.A., Caputo, R., Caraveo, P.A., Castro, D., Chaty, S., Cheung, C.C., Chiaro, G., Cibrario, N., Ciprini, S., Coronado-Blázquez, J., Crnogorcevic, M., Cutini, S., D'Ammando, F., De Gaetano, S., Digel, S.W., Di Lalla, N., Dirirsa, F., Di Venere, L., Domínguez, A., Fallah Ramazani, V., Fegan, S.J., Ferrara, E.C., Fiori, A., Fleischhack, H., Franckowiak, A., Fukazawa, Y., Funk, S., Fusco, P., Galanti, G., Gammaldi, V., Gargano, F., Garrappa, S., Gasparrini, D., Giacchino, F., Giglietto, N., Giordano, F., Giroletti, M., Glanzman, T., Green, D., Grenier, I.A., Grondin, M.-H., Guillemot, L., Guiriec, S., Gustafsson, M., Harding, A.K., Hays, E., Hewitt, J.W., Horan, D., Hou, X., Jóhannesson, G., Karwin, C., Kayanoki, T., Kerr, M., Kuss, M., Landriu, D., Larsson, S., Latronico, L., Lemoine-Goumard, M., Li, J., Liodakis, I., Longo, F., Loparco, F., Lott, B., Lubrano, P., Maldera, S., Malyshev, D., Manfreda, A., Martí-Devesa, G., Mazziotta, M.N., Mereu, I., Meyer, M.,

Michelson, P.F., Mirabal, N., Mitthumsiri, W., Mizuno, T., Moiseev, A.A., Monzani, M.E., Morselli, A., Moskalenko, I.V., Negro, M., Nuss, E., Omodei, N., Orienti, M., Orlando, E., Paneque, D., Pei, Z., Perkins, J.S., Persic, M., Pesce-Rollins, M., Petrosian, V., Pillera, R., Poon, H., Porter, T.A., Principe, G., Rainò, S., Rando, R., Rani, B., Razzano, M., Razzaque, S., Reimer, A., Reimer, O., Reposeur, T., Sánchez-Conde, M., Saz Parkinson, P.M., Scotton, L., Serini, D., Sgrò, C., Siskind, E.J., Smith, D.A., Spandre, G., Spinelli, P., Sueoka, K., Suson, D.J., Tajima, H., Tak, D., Thayer, J.B., Thompson, D.J., Torres, D.F., Troja, E., Valverde, J., Wood, K., Zaharijas, G.: Incremental Fermi Large Area Telescope Fourth Source Catalog. ApJS **260**(2), 53 (2022) https://doi.org/10.3847/1538-4365/ac6751 arXiv:2201.11184 [astro-ph.HE]

19. Mattox, J.R., Bertsch, D.L., Chiang, J., Dingus, B.L., Digel, S.W., Esposito, J.A., Fierro, J.M., Hartman, R.C., Hunter, S.D., Kanbach, G., Kniffen, D.A., Lin, Y.C., Macomb, D.J., Mayer-Hasselwander, H.A., Michelson, P.F., von Montigny, C., Mukherjee, R., Nolan, P.L., Ramanamurthy, P.V., Schneid, E., Sreekumar, P., Thompson, D.J., Willis, T.D.: The Likelihood Analysis of EGRET Data. ApJ **461**, 396 (1996) https://doi.org/10.1086/177068

20. Lott, B., Escande, L., Larsson, S., Ballet, J.: An adaptive-binning method for generating constant-uncertainty/constant-significance light curves with Fermi-LAT data. A&A **544**, 6 (2012) https://doi.org/10.1051/0004-6361/201218873 arXiv:1201.4851 [astro-ph.HE]

21. Giommi, P., Perri, M., Capalbi, M., D'Elia, V., Barres de Almeida, U., Brandt, C.H., Pollock, A.M.T., Arneodo, F., Di Giovanni, A., Chang, Y.L., Civitarese, O., De Angelis, M., Leto, C., Verrecchia, F., Ricard, N., Di Pippo, S., Middei, R., Penacchioni, A.V., Ruffini, R., Sahakyan, N., Israyelyan, D., Turriziani, S.: X-ray spectra, light curves and SEDs of blazars frequently observed by Swift. MNRAS **507**(4), 5690–5702 (2021) https://doi.org/10.1093/mnras/stab2425 arXiv:2108.07255 [astro-ph.HE]

22. Arnaud, K.A.: XSPEC: The First Ten Years. In: Jacoby, G.H., Barnes, J. (eds.) Astronomical Data Analysis Software and Systems V. Astronomical Society of the Pacific Conference Series, vol. 101, p. 17 (1996)

23. Cash, W.: Parameter estimation in astronomy through application of the likelihood ratio. ApJ **228**, 939–947 (1979) https://doi.org/10.1086/156922

24. Middei, R., Giommi, P., Perri, M., Turriziani, S., Sahakyan, N., Chang, Y.L., Leto, C., Verrecchia, F.: The first hard X-ray spectral catalogue of Blazars observed by NuSTAR. MNRAS **514**(3), 3179–3190 (2022) https://doi.org/10.1093/mnras/stac1185 arXiv:2205.05089 [astro-ph.HE]

25. Roming, P.W.A., Kennedy, T.E., Mason, K.O., Nousek, J.A., Ahr, L., Bingham, R.E., Broos, P.S., Carter, M.J., Hancock, B.K., Huckle, H.E., Hunsberger, S.D., Kawakami, H., Killough, R., Koch, T.S., McLelland, M.K., Smith, K., Smith, P.J., Soto, J.C., Boyd, P.T., Breeveld, A.A., Holland, S.T., Ivanushkina, M., Pryzby, M.S., Still, M.D., Stock, J.: The Swift Ultra-Violet/Optical Telescope. Space Sci. Rev. **120**(3-4), 95–142 (2005) https://doi.org/10.1007/s11214-005-5095-4 arXiv:astro-ph/0507413 [astro-ph]

26. Gehrels, N., Chincarini, G., Giommi, P., Mason, K.O., Nousek, J.A., Wells, A.A., White, N.E., Barthelmy, S.D., Burrows, D.N., Cominsky, L.R., Hurley, K.C., Marshall, F.E., Mészáros, P., Roming, P.W.A., Angelini, L., Barbier, L.M., Belloni, T., Campana, S., Caraveo, P.A., Chester, M.M., Citterio, O., Cline, T.L., Cropper, M.S., Cummings, J.R., Dean, A.J., Feigelson, E.D., Fenimore, E.E., Frail, D.A., Fruchter, A.S., Garmire, G.P., Gendreau, K., Ghisellini, G., Greiner, J., Hill, J.E., Hunsberger, S.D., Krimm, H.A., Kulkarni, S.R., Kumar, P., Lebrun, F., Lloyd-Ronning, N.M., Markwardt, C.B., Mattson, B.J., Mushotzky, R.F., Norris, J.P., Osborne, J., Paczynski, B., Palmer, D.M., Park, H.-S., Parsons, A.M., Paul, J., Rees, M.J., Reynolds, C.S., Rhoads, J.E., Sasseen, T.P., Schaefer, B.E., Short, A.T., Smale, A.P., Smith, I.A., Stella, L., Tagliaferri, G., Takahashi, T., Tashiro, M., Townsley, L.K., Tueller, J., Turner, M.J.L., Vietri, M., Voges, W., Ward, M.J., Willingale, R., Zerbi, F.M., Zhang, W.W.: The Swift Gamma-Ray Burst Mission. ApJ **611**(2), 1005–1020 (2004) https://doi.org/10.1086/422091 arXiv:astro-ph/0405233 [astro-ph]

27. Poole, T.S., Breeveld, A.A., Page, M.J., Landsman, W., Holland, S.T., Roming, P., Kuin, N.P.M., Brown, P.J., Gronwall, C., Hunsberger, S., Koch, S., Mason, K.O., Schady, P., vanden Berk, D., Blustin, A.J., Boyd, P., Broos, P., Carter, M., Chester, M.M., Cucchiara, A., Hancock, B., Huckle, H., Immler, S., Ivanushkina, M., Kennedy, T., Marshall, F., Morgan, A., Pandey, S.B., de Pasquale, M., Smith, P.J., Still, M.: Photometric calibration of the Swift ultraviolet/optical telescope. MNRAS **383**(2), 627–645 (2008) https://doi.org/10.1111/j.1365-2966.2007.12563.x arXiv:0708.2259 [astro-ph]

28. Kochanek, C.S., Shappee, B.J., Stanek, K.Z., Holoien, T.W.-S., Thompson, T.A., Prieto, J.L., Dong, S., Shields, J.V., Will, D., Britt, C., Perzanowski, D., Pojmański, G.: The All-Sky Automated Survey for Supernovae (ASAS-SN) Light Curve Server v1.0. PASP **129**(980), 104502 (2017) https://doi.org/10.1088/1538-3873/aa80d9 arXiv:1706.07060 [astro-ph.SR]

29. Bellm, E.C., Kulkarni, S.R., Graham, M.J., Dekany, R., Smith, R.M., Riddle, R., Masci, F.J., Helou, G., Prince, T.A., Adams, S.M., Barbarino, C., Barlow, T., Bauer, J., Beck, R., Belicki, J., Biswas, R., Blagorodnova, N., Bodewits, D., Bolin, B., Brinnel, V., Brooke, T., Bue, B., Bulla, M., Burruss, R., Cenko, S.B., Chang, C.-K., Connolly, A., Coughlin, M., Cromer, J., Cunningham, V., De, K., Delacroix, A., Desai, V., Duev, D.A., Eadie, G., Farnham, T.L., Feeney, M., Feindt, U., Flynn, D., Franckowiak, A., Frederick, S., Fremling, C., Gal-Yam, A., Gezari, S., Giomi, M., Goldstein, D.A., Golkhou, V.Z., Goobar, A., Groom, S., Hacopians, E., Hale, D., Henning, J., Ho, A.Y.Q., Hover, D., Howell, J., Hung, T., Huppenkothen, D., Imel, D., Ip, W.-H., Ivezić, Ž., Jackson, E., Jones, L., Juric, M., Kasliwal, M.M., Kaspi, S., Kaye, S., Kelley, M.S.P., Kowalski, M., Kramer, E., Kupfer, T., Landry, W., Laher, R.R., Lee, C.-D., Lin, H.W., Lin, Z.-Y., Lunnan, R., Giomi, M., Mahabal, A., Mao, P., Miller, A.A., Monkewitz, S., Murphy, P., Ngeow, C.-C., Nordin, J., Nugent, P., Ofek, E., Patterson, M.T., Penprase, B., Porter, M., Rauch, L., Rebbapragada, U., Reiley, D., Rigault, M., Rodriguez, H., van Roestel, J., Rusholme, B., van Santen, J., Schulze, S., Shupe, D.L., Singer, L.P., Soumagnac, M.T., Stein, R., Surace, J., Sollerman, J., Szkody, P., Taddia, F., Terek, S., Van Sistine, A., van Velzen, S., Vestrand, W.T., Walters, R., Ward, C., Ye, Q.-Z., Yu, P.-C., Yan, L., Zolkower, J.: The Zwicky Transient Facility: System Overview, Performance, and First Results. PASP **131**(995), 018002 (2019) https://doi.org/10.1088/1538-3873/aaecbe arXiv:1902.01932 [astro-ph.IM]

30. Kaiser, N., Aussel, H., Burke, B.E., Boesgaard, H., Chambers, K., Chun, M.R., Heasley, J.N., Hodapp, K.-W., Hunt, B., Jedicke, R., Jewitt, D., Kudritzki, R., Luppino, G.A., Maberry, M., Magnier, E., Monet, D.G., Onaka, P.M., Pickles, A.J., Rhoads, P.H.H., Simon, T., Szalay, A., Szapudi, I., Tholen, D.J., Tonry, J.L., Waterson, M., Wick, J.: Pan-STARRS: A Large Synoptic Survey Telescope Array. In: Tyson, J.A., Wolff, S. (eds.) Survey and Other Telescope Technologies and Discoveries. Society of Photo-Optical Instrumentation Engineers (SPIE) Conference Series, vol. 4836, pp. 154–164 (2002). https://doi.org/10.1117/12.457365

31. Mainzer, A., Bauer, J., Grav, T., Masiero, J., Cutri, R.M., Dailey, J., Eisenhardt, P., McMillan, R.S., Wright, E., Walker, R., Jedicke, R., Spahr, T., Tholen, D., Alles, R., Beck, R., Brandenburg, H., Conrow, T., Evans, T., Fowler, J., Jarrett, T., Marsh, K., Masci, F., McCallon, H., Wheelock, S., Wittman, M., Wyatt, P., DeBaun, E., Elliott, G., Elsbury, D., Gautier, T. IV, Gomillion, S., Leisawitz, D., Maleszewski, C., Micheli, M., Wilkins, A.: Preliminary Results from NEOWISE: An Enhancement to the Wide-field Infrared Survey Explorer for Solar System Science. ApJ **731**(1), 53 (2011) https://doi.org/10.1088/0004-637X/731/1/53 arXiv:1102.1996 [astro-ph.EP]

32. Giommi, P., Sahakyan, N., Israyelyan, D., Manvelyan, M.: The Remarkable Predictive Power of Infrared Data of Blazars. ApJ **963**(1), 48 (2024) https://doi.org/10.3847/1538-4357/ad20cb arXiv:2401.10548 [astro-ph.HE]

33. Sahakyan, N., Bégué, D., Casotto, A., Dereli-Bégué, H., Giommi, P., Gasparyan, S., Vardanyan, V., Khachatryan, M., Pe'er, A.: Modeling Blazar Broadband Emission with Convolutional Neural Networks. II. External Compton Model. ApJ **971**(1), 70 (2024) https://doi.org/10.3847/1538-4357/ad5351 arXiv:2402.07495 [astro-ph.HE]

34. Bégué, D., Sahakyan, N., Dereli-Bégué, H., Giommi, P., Gasparyan, S., Khachatryan, M., Casotto, A., Pe'er, A.: Modeling Blazar Broadband Emission with a Convolutional Neural Network. I. Synchrotron Self-Compton Model. ApJ **963**(1), 71 (2024) https://doi.org/10.3847/1538-4357/ad19cf arXiv:2311.02979 [astro-ph.HE]

35. Sahakyan, N., Bégué, D., Casotto, A., Dereli-Bégué, H., Vardanyan, V., Khachatryan, M., Giommi, P., Pe'er, A.: Modeling Blazar Broadband Emission with Convolutional Neural Networks. III. Proton Synchrotron and Hybrid Models. ApJ **990**(2), 222 (2025) https://doi.org/10.3847/1538-4357/adf734 arXiv:2506.23885 [astro-ph.HE]

36. Shakura, N.I., Sunyaev, R.A.: Reprint of 1973A&A....24..337S. Black holes in binary systems. Observational appearance. A&A **500**, 33–51 (1973)

37. Ghisellini, G., Tavecchio, F.: Canonical high-power blazars. MNRAS **397**, 985–1002 (2009) https://doi.org/10.1111/j.1365-2966.2009.15007.x arXiv:0902.0793

38. Gasparyan, S., Bégué, D., Sahakyan, N.: Time-dependent lepto-hadronic modelling of the emission from blazar jets with SOPRANO: the case of TXS 0506 + 056, 3HSP J095507.9 + 355101, and 3C 279. MNRAS **509**(2), 2102–2121 (2022) https://doi.org/10.1093/mnras/stab2688 arXiv:2110.01549 [astro-ph.HE]

39. Feroz, F., Hobson, M.P., Bridges, M.: MULTINEST: an efficient and robust Bayesian inference tool for cosmology and particle physics. MNRAS **398**, 1601–1614 (2009) https://doi.org/10.1111/j.1365-2966.2009.14548.x arXiv:0809.3437

40. Domínguez, A., Primack, J.R., Rosario, D.J., Prada, F., Gilmore, R.C., Faber, S.M., Koo, D.C., Somerville, R.S., Pérez-Torres, M.A., Pérez-González, P., Huang, J.-S., Davis, M., Guhathakurta, P., Barmby, P., Conselice, C.J., Lozano, M., Newman, J.A., Cooper, M.C.: Extragalactic background light inferred from AEGIS galaxy-SED-type fractions. MNRAS **410**(4), 2556–2578 (2011) https://doi.org/10.1111/j.1365-2966.2010.17631.x arXiv:1007.1459 [astro-ph.CO]

41. Sahakyan, N., Gasparyan, S.: High energy gamma-ray emission from PKS 1441+25. MNRAS **470**(3), 2861–2869 (2017) https://doi.org/10.1093/mnras/stx1402 arXiv:1706.01611 [astro-ph.HE]